Fundamental investigations of capacitive radio frequency plasmas: simulations and experiments

Z Donkó[1], J Schulze[2], U Czarnetzki[2], A Derzsi[1], P Hartmann[1], I Korolov[1] and E Schüngel[2]

[1] Institute of Solid State Physics and Optics, Wigner Research Centre for Physics, Hungarian Academy of Sciences, H-1121 Budapest, Konkoly Thege M. str. 29-33, Hungary
[2] Institute for Plasma and Atomic Physics, Ruhr University Bochum, 44780 Bochum, Germany

E-mail: donko.zoltan@wigner.mta.hu

Abstract

Capacitive radio frequency (RF) discharge plasmas have been serving hi-tech industry (e.g. chip and solar cell manufacturing, realization of biocompatible surfaces) for several years. Nonetheless, their complex modes of operation are not fully understood and represent topics of high interest. The understanding of these phenomena is aided by modern diagnostic techniques and computer simulations. From the industrial point of view the control of ion properties is of particular interest; possibilities of independent control of the ion flux and the ion energy have been utilized via excitation of the discharges with multiple frequencies. 'Classical' dual-frequency (DF) discharges (where two significantly different driving frequencies are used), as well as discharges driven by a base frequency and its higher harmonic(s) have been analyzed thoroughly. It has been recognized that the second solution results in an electrically induced asymmetry (electrical asymmetry effect), which provides the basis for the control of the mean ion energy. This paper reviews recent advances on studies of the different electron heating mechanisms, on the possibilities of the separate control of ion energy and ion flux in DF discharges, on the effects of secondary electrons, as well as on the non-linear behavior (self-generated resonant current oscillations) of capacitive RF plasmas. The work is based on a synergistic approach of theoretical modeling, experiments and kinetic simulations based on the particle-in-cell approach.

(Some figures may appear in colour only in the online journal)

1. Introduction

Capacitively coupled radio frequency (CCRF) discharges play a basic role in modern plasma processing technologies: in etching and deposition processes used for e.g. microelectronics and solar cell manufacturing as well as bio-engineering [1, 2]. At smaller size, atmospheric pressure plasma jets (μ-APPJ), driven by radio frequencies (RFs), are of major interest for medical applications [3]. In addition to the interest in their applications in these fields CCRF discharges exhibit rich and complex physics that has attracted lots of attention. Due to the development of modern plasma diagnostics tools and sophisticated modeling

approaches, many of the details of their operation became uncovered.

At RFs, electrons respond to the field variations. If the ion plasma frequency, ω_{pi}, is significantly less than the applied RF, ω_{RF}, the ions move under the influence of the time averaged sheath electric fields. If $\omega_{\text{RF}} \leqslant \omega_{\text{pi}}$, the ion motion is modulated by the instantaneous field. The latter scenario is realized for light ions, low plasma densities and/or low driving frequencies [4–6].

The electron kinetics and the electron heating mode are key properties of RF discharges, since they are the basis of charge reproduction to balance the losses in steady state. While in direct current discharges surface processes are normally

1

necessary for charge reproduction, in RF discharges the oscillating electric field can accelerate electrons to high enough energies to create sufficient ionization in the gas phase to sustain the discharge. This operation mode of RF discharges has traditionally been called the α-mode (named after the 'first Townsend (ionization) coefficient', α, that yields the number of electron–ion pairs created by electrons over a unit length). The dominant contribution to the electron heating is provided by the rapid movement of the electrode sheaths via two mechanisms [7]: (i) stochastic electron heating by the expanding boundary sheaths, which leads to the generation of electron beams, that propagate toward the bulk [8], or to the excitation of waves, if the sheath expands on a timescale faster than the inverse local electron plasma frequency [9]. The sheath motion and, thus, stochastic heating can be significantly enhanced by self-excited non-linear plasma series resonance (PSR) oscillations of the RF current in asymmetric discharges [10–16]. (ii) During sheath contraction field reversals will appear, if the electron transport to the electrode by diffusion is insufficient to compensate the ion flux. The electron transport can be limited by collisions at high pressures, particularly in molecular gases, or by electron inertia at low pressures. Such reversed fields accelerate electrons toward the electrode [17, 18].

In this way RF discharges can operate without ionization by secondary electrons emitted from the electrodes or created by ionization inside the sheaths under distinct conditions and this is, actually, often assumed in discharge models as a simplification. However, secondary electrons contribute usually to the ionization and can even dominate it at high RF voltage amplitudes and/or pressures depending on the electrode material and its emission coefficient, γ [7]. Typical secondary yields of clean metallic electrodes are comparatively small, $0.01 \leqslant \gamma \leqslant 0.1$ (see e.g. [19]), but materials often used in microelectronics, e.g. quartz, have high γ values, reaching $\gamma = 0.4$–0.5 [20]. At high γ values significant electron heating may originate from secondary electrons that are emitted from the electrodes and gain high energies during their flight through the electrode sheath (at times when the sheath is expanded), where they are multiplied by collisions at high pressures. This operation mode is called γ-mode (named after the 'second Townsend coefficient', γ). At atmospheric pressures, e.g. in μ-APPJ-s, the ionization can be dominated by electrons generated by Penning ionization inside the sheaths [3], which is often called γ-mode, too.

While electropositive macroscopic and dust free discharges operate either in α-mode or γ-mode [7], or in their combination, additional electron heating mechanisms show up in electronegative macroscopic plasmas and in atmospheric pressure microdischarges [21]. In such plasmas, the conductivity of the bulk plasma is significantly reduced by either a depleted electron density, collisions or a combination of both. As a result, a higher electric field is required to drive a given current through the bulk plasma. Electrons accelerated in this high field contribute significantly to ionization and excitation. A similar effect is caused by the presence of dust particles in the bulk [22]. Additionally, in electronegative discharges large electron density gradients develop temporarily within the RF period in the electropositive edge region of the discharge. This leads to the generation of ambipolar fields that accelerate electrons as well [21].

In large area CCRF discharges operated at very high-frequencies (VHFs) such as used for solar cell manufacturing, electromagnetic standing wave and skin effects can reduce the radial homogeneity of the ion flux to the substrate [23].

In this paper, we shall review the basics of the operation of macroscopic dust free capacitively coupled RF discharges with relatively small electrode areas and low plasma densities (to safely exclude electromagnetic effects) driven by a superposition of N harmonic voltage waveforms. In this case the voltage drop across the discharge is given by

$$\phi(t) = \eta + \phi_\sim(t) = \eta + \sum_{k=1}^{N} \phi_k \cos(2\pi f_k t + \Theta_k), \quad (1)$$

where η is the dc self-bias voltage, $\phi_\sim(t)$ is the voltage waveform of the generator, with ϕ_k and Θ_k, respectively, being the amplitude and the phase angle of the kth harmonic of frequency f_k. We assume that $f_1 < f_2 < \cdots < f_N$. While different notations have been used in the literature for the amplitudes and frequencies of the different harmonics, for clarity, we shall use the above notation throughout this paper, even when we reproduce earlier results in some of the figures.

Discharges with single-frequency excitation ($N = 1$) have widely been used as plasma sources during several decades. In such discharges, the value of the dc self-bias—which has an important effect on the ion energy distribution at the electrodes—depends considerably on the geometrical parameters of the discharge cell [24]. In most RF plasma sources the powered electrode has a smaller area compared with the grounded electrode, in such cases a negative self-bias develops (see, e.g., [2]). In geometrically symmetrical settings η vanishes.

The separate control of ion properties, namely, *the ion flux*, Γ_i, the *mean ion energy*, $\bar{E}_i$, and the shape of the ion flux energy distribution function at the electrodes, is of paramount importance in plasma processing applications. The ion flux determines the processing rate, whereas the mean ion energy and the shape of the distribution function determine processes at the surfaces. It has been recognized about two decades ago that using discharges excited by two, or even multiple frequencies [25–31] provides an enhanced separate control of ion flux and mean energy as compared with single-frequency discharges. Likewise, hybrid (inductive+capacitive, helicon+capacitive and dc+RF) sources, partly with customized voltage waveforms applied to the substrate to control the shape of the ion distribution function, have been developed to provide an independent control of ion properties [32–36].

In the case of dual-frequency (DF) excitation ($N = 2$) we distinguish two approaches:

(a) 'Classical' DF discharges combine excitation with a high-frequency and a low-frequency component. To a first approximation, the high-frequency voltage amplitude, ϕ_2, controls the plasma density (as the electron heating rate is proportional to the square of the frequency), and consequently, the ion flux to the electrodes. The low-frequency voltage

amplitude, $\phi_1 \gg \phi_2$, on the other hand, controls the mean ion energy. This separate control has shown to be effective if $f_1 \ll f_2$ is ensured, thus, in practice, f_1 is typically in the range of several MHz, and f_2 covers frequencies from tens to hundreds of MHz [25–31]. The effects of phase shifts between the harmonics have been investigated in [37–39], but in most works the phases are assumed to be zero. The separate control of ion properties in such DF discharges is hindered by the coupling of the two frequencies [40–44]; the low-frequency modulation of the sheath length has an influence on the electron heating properties at high-frequency sheath expansion. Additionally, secondary electrons have recently been found to adversely influence the separate control of the ion properties [45, 46].

(b) The electrical asymmetry effect (EAE), proposed in 2008 [47], has proven to be an efficient alternative way to control ion properties. Discharges under EAE conditions are normally driven by a superposition of harmonic RF waveforms of a fundamental and a second harmonic frequency, i.e. in (1), $N = 2$, $f_2 = 2f_1$. It has been predicted by modeling and simulations [47, 48], and later confirmed experimentally [49] that due to the (generally) asymmetric waveform of $\phi_\sim(t)$ a dc self-bias voltage develops in the discharge, even if the electrode configuration is geometrically symmetrical. By changing the phases of the harmonics the self-bias voltage and the mean sheath voltages can be changed, which, in turn, leads to different energy distributions of ions reaching the two electrodes. The control parameters for the ion energy are, thus, the phases, or the phase difference $\Theta_1 - \Theta_2$. We note that most of the past papers on the EAE have varied Θ_1 and set $\Theta_2 = 0$, and used the notation $\Theta = \Theta_1$. The maximum negative and positive value of the self-bias occurs at (or near) $\Theta = 0°$ and $\Theta = 90°$, respectively. The ion flux has proven to exhibit little sensitivity on the phase variation at fixed voltage amplitudes. Reaching a high self-bias has been found to be advantageous as this provides a wider range to control the energy of ions at the electrodes. Thus, most of the optimization studies of the EAE have been focused on increasing the value of the self-bias [50, 51].

The EAE has been investigated in different gases, mostly in argon [50–52], but also in hydrogen [53], oxygen [54], and in CF_4 [55]. Optimization of the ratio of the voltage amplitudes (ϕ_2/ϕ_1) was reported in [50]. The effect of secondary electrons has been investigated in [56], in comparison with classical DF discharges. The possibilities of using more than two driving frequencies $(N > 2)$ have been explored in [51]. In this latter work it has been shown that in order to drive η to its two extremes one should (i) set all phase angles to $\Theta_k = 0°$ to reach the highest negative η value and (ii) the phases of odd harmonics to $\Theta_k = 0°$ and the phases of even harmonics to $\Theta_k = 180°$, to reach the highest positive η value. This idea of tailoring a waveform via the EAE, i.e. using multiple harmonics, has been proven experimentally to be a promising approach for film deposition purposes [33, 57] in high density remote plasmas with a capacitively biased substrate. Consequences of using non-sinusoidal driving voltage waveforms on the electron heating have been discussed based on simulations in [58]. Furthermore, unique

opportunities to self-excite PSR oscillations [15, 16] and to manipulate the distribution of particles in dusty plasmas [59] via the EAE have been revealed and are current topics of investigation.

In this paper, we present an overview of the different electron heating mechanisms introduced above and elaborate the main features of both classical DF and EAE discharges. Section 2 describes the different methods used for our study: the simulation approach, the analytical model of capacitive discharges, as well as the experimental setup and diagnostics. Results are presented in section 3, which is divided into three different parts corresponding to three different ways of capacitive discharge excitation: (i) single-frequency, (ii) 'classical' dual-frequency and (iii) electrically asymmetric multi-frequency discharges. Finally, a brief summary is given in the section 4.

2. Methods

The forthcoming parts of the paper briefly review the methods of our investigations: the numerical and analytical approaches as well as the experimental methods.

2.1. Particle-in-cell simulation of radiofrequency discharges

The particle-in-cell (PIC) method represents the most widespread simulation technique for the kinetic description of RF plasma sources. The method, which belongs to the class of 'particle-mesh' approaches, was introduced in the 1960s and has evolved significantly during the following decades [60, 61]. The idea of using a computational mesh avoids the need to account for the pairwise interaction of all individual particles. In addition to this, the use of 'superparticles', which represent a large number of real particles, brings the number of particles in the simulation into a tractable order of magnitude. While the PIC scheme can account for electromagnetic effects [23], here we restrict ourselves to electrostatic simulations.

In studies of low-pressure discharges collisions have to be incorporated in the simulations; this is usually accomplished by the Monte Carlo method. The simulation scheme resulting from this combination of the techniques is referred to as the 'PIC/MCC' approach [62]. For electropositive noble gas discharges, elastic scattering, excitation and ionization processes are typically considered for the electrons. For electron–atom collisions the cold gas approximation is commonly used. For ions it is usually sufficient to take into account elastic collisions, except at high voltages, where excitation and ionization may as well occur in ion–atom collisions. Concerning elastic ion–atom collisions we use cross sections for an isotropic part and a backward scattering part [63]. We note that a similar approach has been developed in [64] for studies of electron transport.

In the simulations of molecular gases several electron–molecule processes have to be accounted for and a number of different ionic species have to be traced. In our simulations of CF_4 discharges we include a fairly complete set of electron-impact processes (elastic momentum transfer, vibrational and electronic excitation, dissociative ionization, attachment and
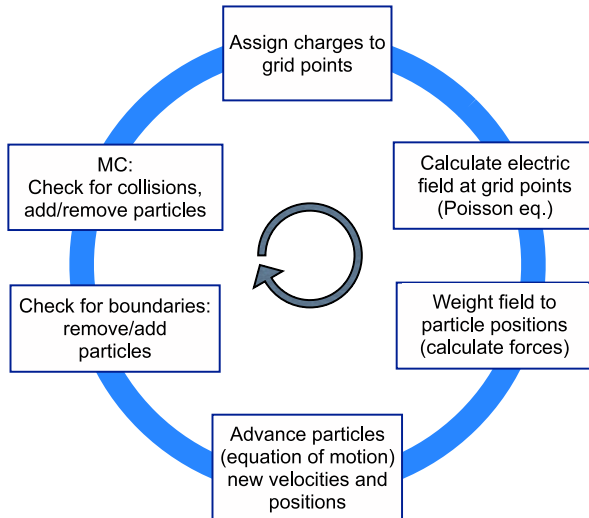
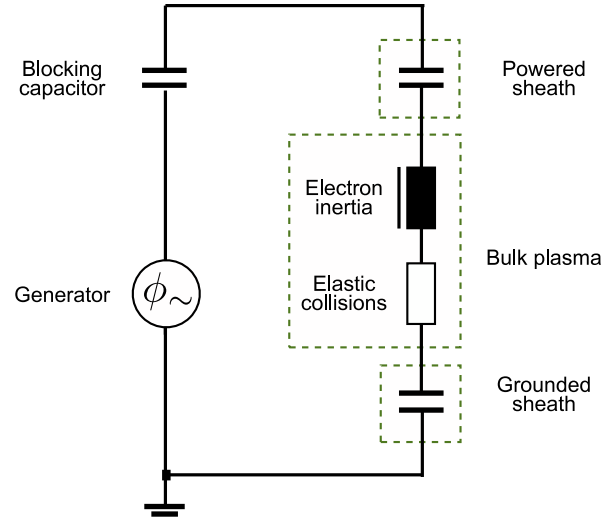**Figure 1.** The PIC/MCC cycle for bounded, collisional discharge plasmas.

Figure 2. Equivalent electrical circuit of a CCRF discharge.

neutral dissociation channels). The set of processes is based on [65]. We trace the dominant ions: CF_3^+, CF_3^- and F^-; for these species we include a set of ion-molecule reactions, as well as electron–ion and ion-ion recombination channels. In our simplified chemistry model we do not trace, however, neutral radicals and we do not account for the formation of molecules of higher weight. For a complete description of our model see [66].

The PIC/MCC simulations presented here are of 1d3v type (one-dimensional in space, and three-dimensional in velocity space) and are voltage-driven (the time-dependent potential values at the electrodes are used as boundary conditions).

For *bounded* and *collisional* discharge plasmas of interest here, the PIC/MCC simulation cycle consists of the following steps [62, 67–69] (also shown in figure 1):

(1) at each time step the charge of the superparticles (which can be situated at any position inside the discharge gap) is assigned to a grid;

(2) the Poisson equation is solved on the grid: the potential distribution is calculated from the charge distribution, taking into account the potentials applied to the electrodes as boundary conditions;

(3) the forces acting on the particles are obtained by interpolation of the electric field (resulting from the differentiation of the potential) to the positions of the particles;

(4) the new positions and velocities of the particles are obtained from the solution of the equation of motion;

(5) due to the finite volume of the plasma the interaction of the particles with the surrounding surfaces (e.g. reflection, absorption, secondary emission) is accounted for;

(6) collisions between the traced charged particles with each other and with the atoms of the background gas are checked for and are executed.

It is noted that the kinetic properties of the PIC method are negatively affected by the inclusion of the collisions [70]. Nonetheless, PIC/MCC simulations provide a detailed insight into the physics of RF plasma sources by delivering spatio-temporal distributions of quantities of interest: particle distribution functions, the ionization and excitation rates, the electron heating rate, as well as the fluxes and densities of different species. The constraints/requirements for the setting of the parameters in PIC/MCC simulations (grid division, time step, etc) have been discussed in several works, e.g. [71, 72].

Finally we note that the null-collision method is commonly used in PIC/MCC simulations, to speed up computations. This avoids the need for checking the collision probability of each particle with the background gas in each time step. Instead of this, the number of particles to participate in a collision after a time step Δt (including the option for a null-collision) is obtained as

$$N_{\text{coll}} = N_0[1 - \exp(-\nu^* \Delta t)], \tag{2}$$

where N_0 is the number of particles of a given kind (electrons or ion species). ν^* is the total, energy-independent collision frequency that includes the frequency of the null-collision events. For more details see, e.g., [72].

2.2. Analytical model

The (analytical) modeling of the discharge dynamics and electrical behavior of CCRF plasmas has been an intense research topic in the last decades. Numerous mathematical descriptions have been developed, covering the global characteristics, plasma impedance, or, in particular, the sheath dynamics (see, e.g., [31, 73–84] and references therein).

We use the following simple model: For typical conditions of interest here, an equivalent circuit displayed in figure 2 can be associated with a CCRF discharge (see e.g. [11, 47, 85], which describe the analytical model discussed here in deep details). The RF generator is represented by an ideal voltage source, which generates a sinusoidal voltage waveform or the superposition of N sinusoidal waveforms, $\phi_\sim(t)$ (as given by equation (1)). The generator is coupled to the discharge via a blocking capacitor. The circuit reflects the sheaths and bulk structure of the discharge.

The dc voltage drop over the blocking capacitor compensates for the self-bias voltage η that develops over the discharge. The blocking capacitor, on the other hand, usually represents a small impedance for the driving frequencies, allowing us to neglect the ac voltage drop on it. Thus, the voltage balance for the circuit reads

$$\phi_\sim(t) + \eta = \phi_{sp}(t) + \phi_b(t) + \phi_{sg}(t), \qquad (3)$$

where $\phi_{sp}(t)$ and $\phi_{sg}(t)$, respectively, are the sheath voltages at the powered and the grounded electrodes, and ϕ_b is the voltage drop over the plasma bulk.

Generally, the dynamics of both sheaths are $180°$ out of phase, i.e. when the powered electrode sheath voltage is maximum in magnitude, $\phi_{sp} = \hat{\phi}_{sp} < 0$, the absolute value of the grounded electrode sheath voltage is minimum in magnitude, and vice versa. This minimum corresponds to the floating potential, ϕ_{sg}^f. At the times of maximum and minimum applied voltage, when these extremes of the sheath voltages occur, the bulk voltages, $\phi_{b,max}$, $\phi_{b,min}$, differ by their sign and can have different absolute values.

Combining these assumptions with the voltage balance (equation (3)) at the times of maximum and minimum applied voltage and the symmetry parameter, defined as

$$\varepsilon = \left| \frac{\hat{\phi}_{sg}}{\hat{\phi}_{sp}} \right|, \qquad (4)$$

yields an analytical expression for the dc self-bias [51, 85]:

$$\eta = -\frac{\phi_{\sim max} + \varepsilon \phi_{\sim min}}{1 + \varepsilon} + \frac{\phi_{sp}^f + \varepsilon \phi_{sg}^f}{1 + \varepsilon} + \frac{\phi_{b,max} + \varepsilon \phi_{b,min}}{1 + \varepsilon}$$

$$\cong -\frac{\phi_{\sim max} + \varepsilon \phi_{\sim min}}{1 + \varepsilon}. \qquad (5)$$

This result shows that a non-zero dc self-bias will develop even in a geometrically symmetric discharge ($\varepsilon \cong 1$), if we apply a waveform, for which $\phi_{\sim max}$ and $|\phi_{\sim min}|$ are not equal. This can be realized by applying two harmonics with $f_2 = 2f_1$ and improved using more consecutive harmonics with $f_k = kf_1$.

In asymmetric ($\varepsilon \neq 1$) discharges, PSR oscillations of the RF current at frequencies higher than the driving frequencies are observed. Their self-excitation is also understood by this model: all voltage drops in equation (3) can be expressed as a function of the normalized charge in the powered sheath, $q(t) = Q_{sp}(t)/Q_{sp,max}$ with $Q_{sp,max} = A\sqrt{-2e\epsilon_0 \bar{n}_s \hat{\phi}_{sp}}$ being the maximum charge in the powered sheath. Here A is the electrode area and $\bar{n}_s$ is the spatially averaged-ion density within the sheath [85].

The sheaths adjacent to the electrodes can be modeled by non-linear capacitors. The non-linearity arises from the fact that the charge–voltage relations of the sheaths are non-linear, since the sheath widths change as a function of the voltage drop across the sheath, $\phi_s(t)$, in contrast to a capacitor with fixed distance between its electrodes. Therefore, in a sheath with a quasi-static ion density the voltage depends on the charge, $Q_s(t)$, squared, i.e. $|\phi_s(t)| \propto Q_s^2(t)$, [11]. Normalizing all voltages by the total amplitude of the applied voltage,

$$\phi_{tot} = \sum_{k=1}^{N} \phi_k, \qquad (6)$$
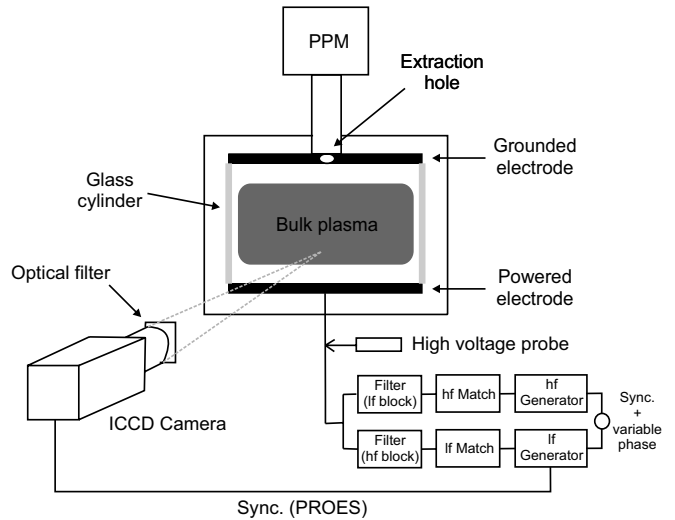
Figure 3. Experimental setup illustrating the electrical network and the diagnostics tools used in our measurements.

and the charge by $Q_{sp,max}$, we obtain

$$\bar{\phi}_{sp}[q(t)] = -q^2(t) \quad \text{and} \quad \bar{\phi}_{sg}[q(t)] = \varepsilon[q_t - q(t)]^2 \qquad (7)$$

under the assumption that the total uncompensated charge, q_t, is split into the net charges in the two sheaths.

The voltage drop across the bulk can be derived from the electron momentum balance equation in the plasma bulk [11, 85]. Based on the assumption that the current, I, in the plasma bulk is purely conduction current, since the driving frequencies are much lower than the electron plasma frequency, the following result for ϕ_b is obtained [15, 85]:

$$\phi_b(t) = -\frac{L}{\bar{A}} \frac{m}{e\bar{n}_b} \left(\frac{\partial}{\partial t} + \nu \right) I(t), \qquad (8)$$

where L is the bulk length, m is the electron mass and ν is the electron-neutral elastic collision frequency. $\bar{n}_b$ and $\bar{A}$ denote effective values of the electron density and bulk area, respectively (see [11]). The first term on the rhs of (8) represents electron inertia ($\propto \partial^2 q/\partial t^2$) and the second term the resistivity ($\propto \partial q/\partial t$) of the quasi-neutral region.

Inserting the expressions for the charge–voltage dependences of the sheaths and bulk into the voltage balance (equation (3)) yields a simplified equation for the charge, q, and via its temporal derivative for the current [15, 85]:

$$\bar{\phi}_\sim(t) + \bar{\eta} = -q^2(t) + \varepsilon[q_t - q(t)]^2 - 2\beta^2 \left[\frac{\partial^2}{\partial t^2} + \nu \frac{\partial}{\partial t} \right] q(t), \qquad (9)$$

where $\beta = \sqrt{A_p L \hat{\phi}_{sp} \epsilon_0 m/(\bar{A}\hat{s}_p \phi_{tot} e^2 \bar{n}_b)}$ is a constant that depends on the discharge geometry and conditions. $\hat{s}_p$ is the maximum extension of the sheath adjacent to the powered electrode. The bars above the voltages on the lhs of (9) represent normalization with respect to ϕ_{tot}.

Equation (9) describes externally driven oscillations of the charge $q(t)$. The important point to note here is the quadratic sheath non-linearity q^2, which is of key importance for the occurrence of the PSR oscillations. If $\varepsilon = 1$
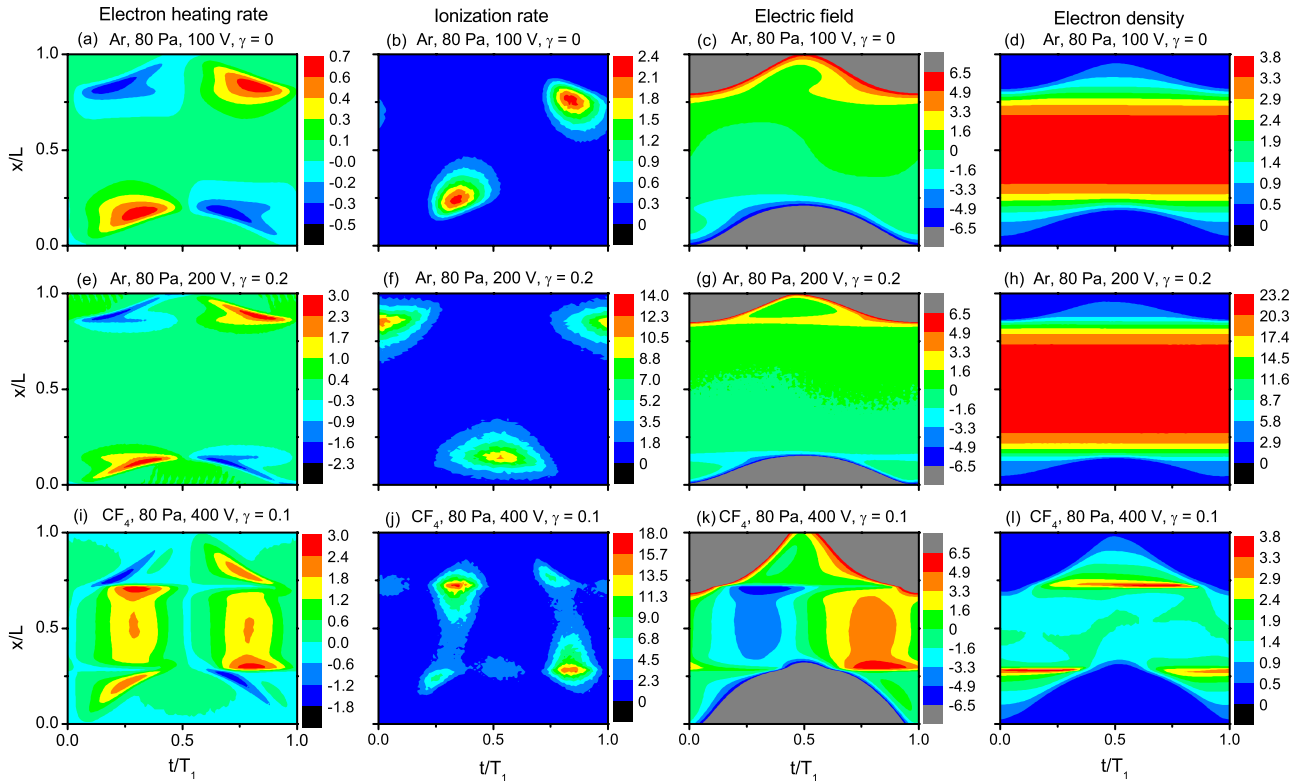
Figure 4. PIC/MCC simulation results: spatio-temporal plots of the electron heating rate (first column), ionization rate (second column) electric field (third column) and electron density (fourth column) in Ar and CF_4 discharges driven at $f_1 = 13.56$ MHz, $p = 80$ Pa with an electrode gap of $L = 1.5$ cm. First row: Ar, $\phi_1 = 100$ V, $\gamma = 0$. Second row: Ar, $\phi_1 = 200$ V, $\gamma = 0.2$. Third row: CF_4, $\phi_1 = 400$ V, $\gamma = 0.1$. The color scales are given in units of 10^5 W m^{-3} (heating rate), 10^{21} m^{-3} s^{-1} (ionization rate), 10^3 V m^{-1} (electric field) and 10^{15} m^{-3} (electron density). The electric field in the sheaths is not resolved due to its higher values. Reproduced from [21].

(total symmetry) the non-linearity q^2 vanishes and a simple, harmonic oscillator equation in q results. Under such conditions q oscillates like $\phi_\sim$ without higher harmonics. Therefore, PSR oscillations cannot occur in conventional geometrically symmetric discharges ($A_p/A_g = 1$), with equal sheath properties ($\varepsilon = 1$). In the case of a strong asymmetry ($\varepsilon < 1$) PSR oscillations may develop, especially at low pressures (typically below $\sim$10 Pa), when the bulk part is dominated by the inductive component and the PSR oscillations are not damped significantly by collisions. Such oscillations of the RF current are theoretically known to enhance ohmic and stochastic heating in CCRF discharges by non-linear electron resonance heating (NERH) [12–14] and can lead to higher electron densities.

2.3. Experimental methods

In the experiments reported here the RF voltage provided by the generator is fed to the discharge cell via a matching network that ensures an optimum power transfer to the plasma. In the case of DF excitation, such as illustrated in figure 3, two generators, two amplifiers and two matching boxes are used. Behind each matchbox a filter prevents the given harmonic from entering the other matching branch. Having passed through the filters, both waveforms are added and applied to one electrode.

The discharge is located inside a Gaseous Electronics Conference (GEC) cell. The radius of both electrodes

(powered and grounded) is 5 cm. The gap between the electrodes is variable (1–2.5 cm). The plasma is shielded from the outer grounded chamber walls by a glass cylinder to improve its geometric symmetry.

Figure 3 also includes schematically the diagnostics tools used in our studies: the optical setup for the phase resolved optical emission spectroscopy (PROES) and a plasma process monitor (PPM) used in the measurements of the flux and the energy distribution of ions reaching the grounded electrode.

The voltage across the discharge is measured by a LeCroy high voltage probe about 1.5 m in front of the powered electrode. The RF period average of the measured voltage yields the dc self-bias. In the case of DF excitation the amplitudes of the individual harmonics are determined by Fourier analysis of the measured waveform. Due to reflection on the cable, the voltage amplitudes and the phase between the harmonics are different at the electrode and at the original position in front of the electrode, where the voltage is measured during plasma operation. Thus, a calibration procedure described in [49] is used to determine the voltage amplitudes and phase at the electrode.

The ion energy and flux at the grounded electrode are measured by a Balzers PPM 422. This device is a combination of an ion energy and mass filter. Here, the PPM is used as an energy filter at fixed mass. A fraction of the ions accelerated toward the grounded electrode by the voltage drop across the adjacent sheath enter the PPM through an extraction hole of
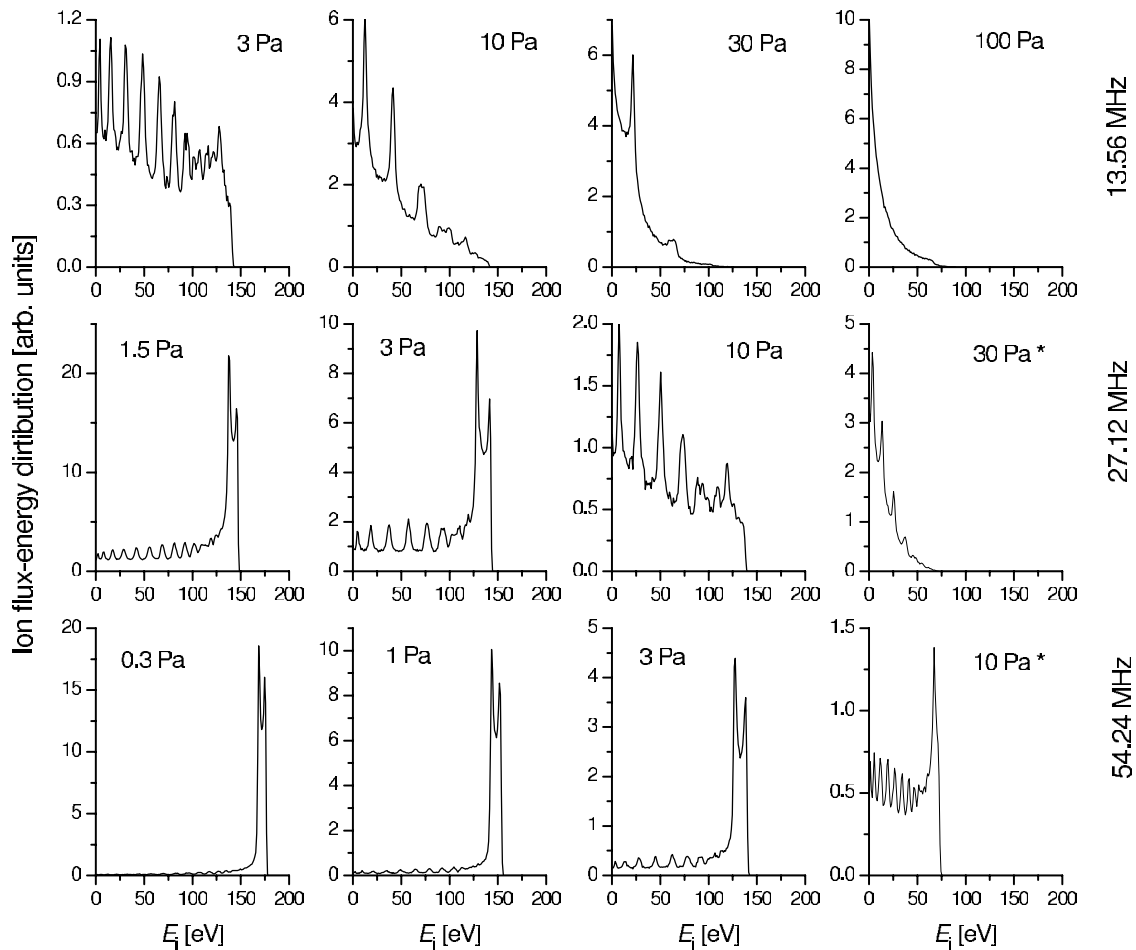
Figure 5. Flux-energy distributions of Ar$^+$ ions reaching the electrodes in single-frequency discharges operated at different frequencies (as indicated for the different rows of panels) and gas pressures (indicated in each panel). The RF voltage is $\phi_1 = 300$ V for all cases except for the cases, where an asterisk appears at the pressure value; in these two cases $\phi_1 = 150$ V, as a convergent solution was not found at $\phi_1 = 300$ V.

diameter 100 μm. These ions are focused on the entrance of the energy filter (Cylindrical Mirror Analyser) by a system of ion optics lenses. Behind this filter the remaining ions of specific energy enter a quadrupole mass filter to extract only ions at a specific mass. The remaining ion beam is reflected by 90° and is detected by a secondary electron multiplier. Here, only singly charged argon ions (40 amu) are detected. The internal pressure of the PPM must be lower than 10^{-3} Pa in order to avoid collisions of ions inside the device that would distort the measurements. This constraints the maximum pressure in the chamber to about 20 Pa, if no additional pumping stages are used. The PPM is calibrated carefully with respect to its energy scale as well as the shape of the measured ion flux-energy distribution functions following a procedure described in [49].

The emission from a specifically chosen neon state (Ne2p1) is measured space and phase resolved within the RF period by PROES [17]. This diagnostic is described in detail in, e.g., [86]. Typically ≈10% neon has to be admixed to the buffer gas for the optical measurements. The emission at 585.5 nm is measured by an Andor Istar ICCD camera synchronized with the low-frequency voltage waveform in combination with an interference filter. From the emission the excitation is calculated using a simple collisional–radiative

model, for more details see [86]. The amount of Ne admixture is a compromise between the intensity of the signal and the degree of perturbation of the discharge. As the ionization potential of Ne is significantly higher than that of Ar, we do not expect a significant influence of Ne on the discharge, and believe that the qualitative comparison with simulation results, obtained for a pure Ar discharge, is meaningful.

3. Results

3.1. Single-frequency discharges

As it has already been emphasized in section 1, the electron heating mode is a key characteristic of RF discharges. Here, we shall briefly illustrate the prominent differences between the specific heating modes. For that we compare three different discharges. In two of these cases the discharges are electropositive (operated in Ar) and the secondary electron emission yield of the electrodes is varied. In the third case we take an electronegative gas, CF$_4$. RF discharges in this gas are known to change from electropositive behavior at low pressures to electronegative character at high pressures [87, 88].

Figure 4 shows PIC/MCC simulation results for these discharges, operated at 80 Pa gas pressure, $L = 1.5$ cm electrode gap and $T_g = 350$ K neutral gas temperature. In these calculations, and also in all the other simulations presented in this paper, the electrons reaching the electrodes are supposed to be reflected elastically, with a probability of 0.2 (called the 'electron reflection coefficient'). Different columns of the figure display spatio-temporal distributions of the electron heating rate, the ionization rate, the electric field and the electron density, within one RF cycle ($f_1 = 13.56$ MHz).

The first and second rows correspond to Ar discharges in α-mode ($\gamma = 0$, $\phi_1 = 100$ V) and γ-mode ($\gamma = 0.2$, $\phi_1 = 200$ V), respectively. In the α-mode dominant patterns in the electron heating rate are seen at phases of sheath expansion. Subsequently, these energetic electrons lead to ionization maxima while traveling toward the discharge center. In the γ-mode, many electrons gain little energy during the phase of sheath expansion, as it can be observed in the respective plot. However, the dominant part of the ionization occurs inside and in front of the expanded sheaths due to the strong acceleration of the relatively small number of γ-electrons, which are emitted form the electrodes, by the strong electric field. In both cases, the electron density decreases monotonically from the discharge center toward the electrodes.

The third row shows results for a CF_4 discharge, where ionization inside the bulk and at the collapsing sheath edge is observed ($\gamma = 0.1$, $\phi_1 = 400$ V). In contrast to the electropositive discharges, the electron heating, as well as the ionization rate and the electric field are high inside the bulk at distinct times within one RF period, as a consequence of the low conductivity due to a low electron density. Maxima of the electron density occur at the sheath edges at times of small sheath width to ensure quasineutrality in the electropositive edge region of the discharge. The ionization rate increases toward the electrode, where the sheath is collapsing, and peaks close to the position of maximum electron density. The heating mode characterized by these features has been termed as the 'drift-ambipolar' (DA) mode [21].

Single-frequency discharges can be operated over a wide range of discharge conditions: excitation frequency and voltage, electrode gap and gas pressure. The electron heating mode, as explained above, largely depends on these parameters as well as on the nature of the gas and the electron emitting properties of the electrodes. Therefore, a wide variety of plasma characteristics and compositions can be realized; a detailed survey of these is, however, far beyond the scope of this paper.

Next, we demonstrate how the flux-energy distribution of the ions reaching the electrodes depends on the operating conditions. For these studies we simulate discharges in argon, at pressures between $p = 0.3$ Pa and 100 Pa, running at frequencies between $f_1 = 13.56$ and 54.24 MHz. The electrode gap is fixed at $L = 2.5$ cm, and the gas temperature is set to $T_g = 350$ K. The secondary yield is $\gamma = 0.1$ for all cases, resulting in a dominating α-mode operation for most of the discharge conditions; contributions of γ-heating show up only at the lowest frequency and at the higher pressure and/or voltage values.
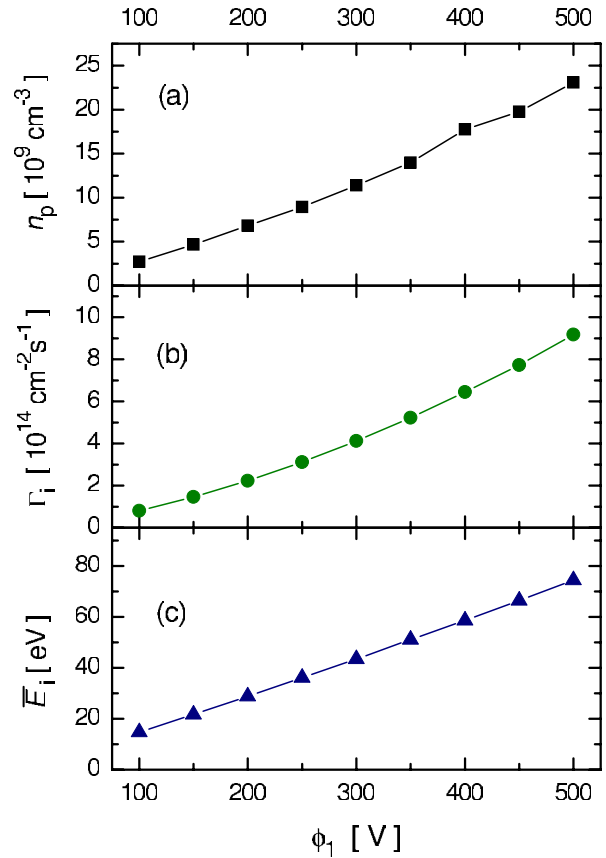

Figure 6. Effect of the RF voltage amplitude, ϕ_1, on the peak bulk ion density (*a*), the temporal average of the ion flux (*b*) and the mean ion energy (*c*) in a single-frequency argon discharge operated at $p = 10$ Pa, $L = 2.5$ cm, $f_1 = 13.56$ MHz.

At $f_1 = 13.56$ MHz the ion flux-energy distributions take complicated shapes at low pressures. Multiple peaks in the distribution appear due to a combined effect of periodic acceleration of ions in the sheaths (the ion transit time is longer than the period of the RF waveform) and of charge exchange collisions [89]. With increasing pressure more and more collisions take place, i.e. the ion mean free path λ_i becomes much shorter than the sheath width s. Consequently, the probability of ions undergoing many collisions in the sheath is high compared with the probability of few or no collisions, leading to an almost exponentially decreasing ion flux as a function of the ion energy. At $f_1 = 27.12$ MHz the ion flux-energy distributions at high pressures are similar to those at low pressures at 13.56 MHz. This is caused by an increase in the plasma density as a function of frequency at fixed driving voltage amplitude. Thus, the sheath widths are reduced and the ratio λ_i/s_{max}, i.e. the collisionality of the sheath, is similar compared with lower pressures at 13.56 MHz. At fixed frequency λ_i/s_{max} increases at lower pressure, so that the sheaths become more collisionless and the ion flux-energy distribution functions tends toward a single peak at high energies (figure 5).

Despite the fact that various ion flux-energy distributions can be realized in single-frequency discharges, an independent control of the ion flux and mean ion energy cannot be achieved in a straightforward manner. In a discharge, which is operated
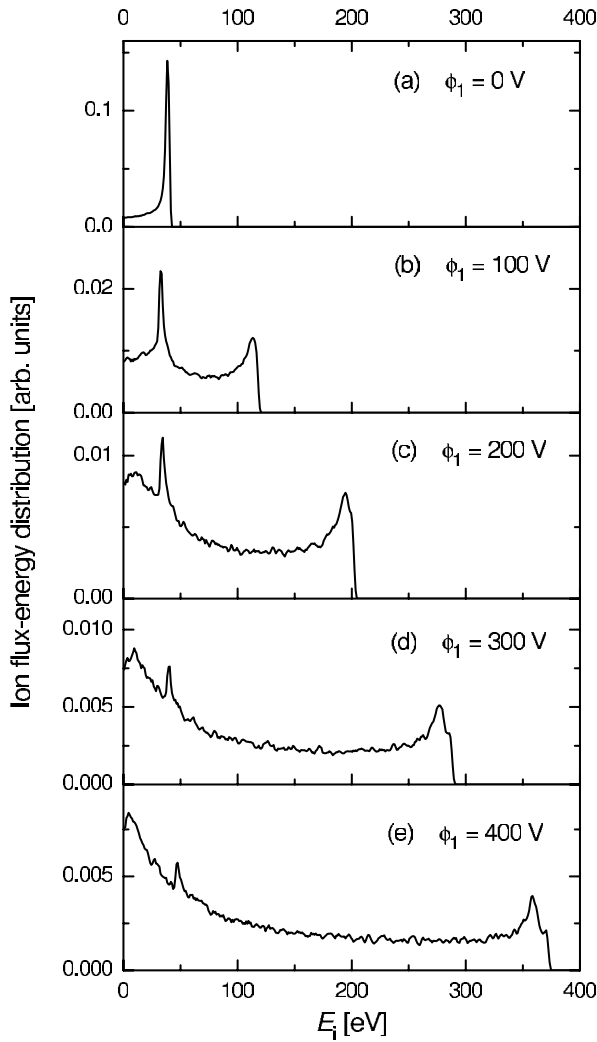
Figure 7. Flux-energy distributions of Ar$^+$ ions obtained in PIC/MCC simulations of classical dual-frequency discharges operated at $f_1 = 1$ MHz and $f_2 = 100$ MHz, as a function of ϕ_1. The amplitude of the high-frequency voltage is fixed at $\phi_2 = 60$ V. $p = 3.33$ Pa, $L = 2$ cm, $\gamma = 0$.

at a fixed pressure, the change in the discharge voltage influences both the bulk ion density (and consequently the ion flux) and the mean ion energy (via the changing sheath voltage). This effect is illustrated in figure 6, which shows the above characteristics in a single-frequency argon discharge at $p = 10$ Pa, $L = 2.5$ cm, $f_1 = 13.56$ MHz.

Figure 6 clearly shows that the ion density and the ion flux are strongly correlated, both change by a factor of about 10 within the range 100 V $\leqslant \phi_1 \leqslant 500$ V. At the same time, the mean ion energy changes by a factor of 6. This interdependency of plasma properties in single-frequency discharges has motivated the development of sources operating at two or multiple frequencies, which will be discussed in the forthcoming parts of this paper.

3.2. Classical DF discharges

Classical DF discharges operate typically at $f_1 \ll f_2$, so that one expects the plasma density and the ion flux to be
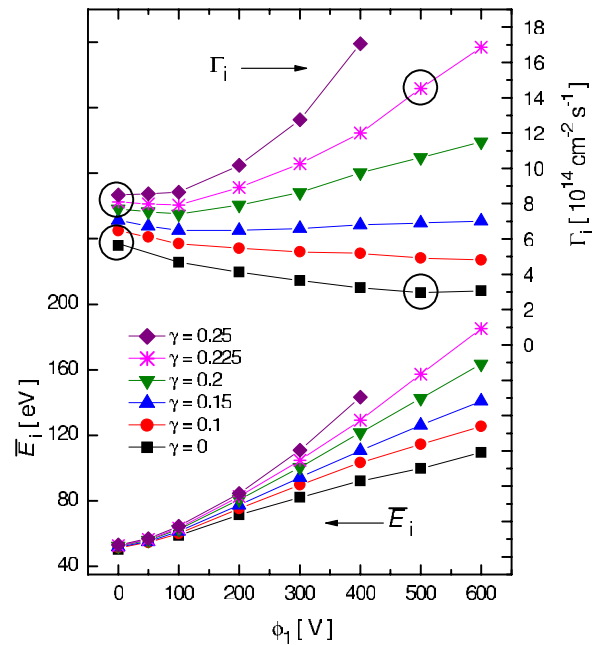

Figure 8. Mean ion energy (left scale, lower set of curves) and ion flux (right scale, upper set of curves) in 'classical' DF discharges in argon, $f_1 = 1.937$ MHz and $f_2 = 27.12$ MHz, for various secondary yields. The conditions marked by the black circles are further analyzed. Partly reproduced with permission from [46]. Copyright by AIP.

defined by the high-frequency voltage amplitude ϕ_2, whereas the low-frequency voltage amplitude, $\phi_1 \gg \phi_2$, is the control parameter for the mean ion energy. The shape of the ion flux-energy distribution largely depends on the relation between the ion transit time through the sheath (τ_i) and the periods of the driving frequencies. For an efficient control of the ion properties $T_2 = 1/f_2 < \tau_i < T_1 = 1/f_1$ is favorable. In figure 7 we display flux-energy distributions of Ar$^+$ ions in discharges, where this relation is fulfilled, as driving frequencies of $f_1 = 1$ MHz $\ll f_2 = 100$ MHz are chosen. The amplitude of the high-frequency harmonic is fixed at $\phi_2 = 60$ V. The discharge is operated at $p = 3.33$ Pa and $L = 2$ cm. We assume $T_g = 300$ K and $\gamma = 0$.

At $\phi_1 = 0$ V the sheaths are narrow and almost collisionless, since a relatively high charged particle density is produced via the high-frequency voltage, resulting in a small sheath width. The ion energy distribution sharply peaks at about $\cong 45$ eV. The upper limit of the ion energies smoothly extends toward higher values as ϕ_1 is increased. We note that an increasing number of ions arrive with very low energies, too, which is the result of the increasing sheath widths at higher ϕ_1.

Regarding the effect of ϕ_1 on the ion flux, different conclusions were drawn in previous studies. In Ar/CF$_4$/N$_2$ discharges a complicated behavior of the ion flux as a function of ϕ_1 was observed, depending on the applied frequencies [90]. Neglecting secondary electrons, in [44] and [66], a decrease in the ion flux with increasing ϕ_1 was observed for Ar and Ar/CF$_4$ discharges. In the studies reported in [91] the ion flux was found to remain nearly constant, regardless of ϕ_1. In a recent experiment, on the other hand, the flux was found to increase as a function of ϕ_1 in a discharge operated at 1.937 and 27.12 MHz
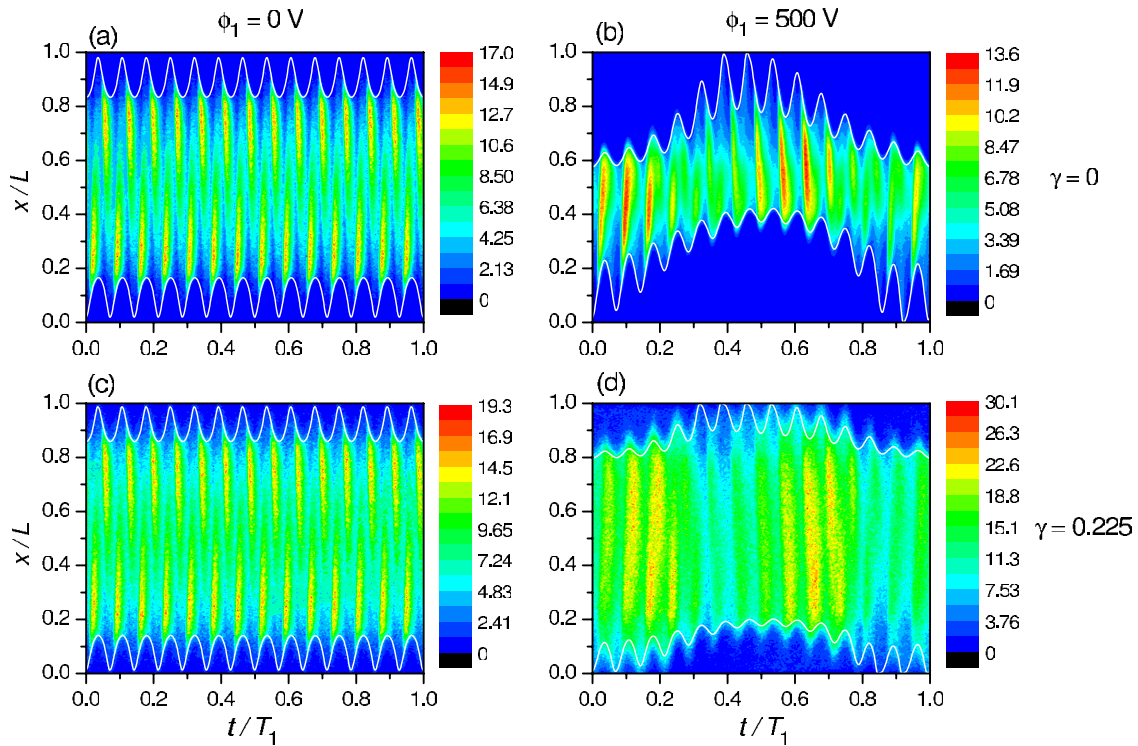
Figure 9. Spatio-temporal distribution of the ionization rate within one period of the fundamental frequency for different combinations of ϕ_1 and γ at 6.6 Pa (units are 10^{14} cm^{-3} s^{-1}). The powered electrode is situated at $x = 0$. $L = 2.5$ cm, $\phi_2 = 200$ V. The white lines indicate the sheath edges. Reproduced with permission from [46]. Copyright by AIP.

in a mixture of argon and oxygen [45]. To resolve these, seemingly contradicting, observations we have carried out a systematic study of the effects of secondary electrons in DF discharges operated at $f_1 = 1.937$ MHz and $f_2 = 27.12$ MHz ($f_2/f_1 = 14$) [46].

Figure 8 shows the mean ion energy and the ion flux as a function of the low-frequency voltage amplitude ϕ_1 (which used to be the control parameter for the ion energy). The results confirm that this parameter allows tuning $\bar{E}_i$ over a wide range. On the other hand, depending on the secondary electron yield, different results for $\Gamma_i(\phi_1)$ are obtained. At zero and small γ values the ion flux decreases as a function of ϕ_1; these data confirm the results of some of the earlier calculations [66]. At high γ values an opposite behavior, an increase in the flux with ϕ_1 is observed, confirming the experimental observations in discharges with oxidized electrodes [45] that can be characterized with a high secondary yield. The ion flux stays reasonably constant only at intermediate γ values. This result points out the difficulty of controlling ion properties independently in classical DF discharges.

The four data points marked with circles in figure 8 are further analyzed. Figure 9 shows the spatial and temporal distribution of the ionization rate in the discharges at these four parameter combinations. Looking at the $\gamma = 0$ cases we observe that the sheaths are significantly expanded when the low-frequency voltage amplitude is increased (compare panels (*a*) and (*b*)). The high-frequency sheath motion is coupled to the extension of the sheaths caused by the low-frequency voltage. Therefore, around the phases of minimum and maximum of the applied low-frequency voltage, the high-frequency sheath edge of the powered and grounded sheaths,

respectively, oscillates with a smaller amplitude due to the higher ion density found further from the electrodes. This frequency coupling results in a smaller value of the space and time-integrated ionization rate, and consequently, in a smaller ion density and ion flux. At $\gamma = 0.225$ the same change in ϕ_1 has an opposite effect on the ion flux, which can be explained by the enhanced multiplication of electrons emitted from the electrode in phases, when both ϕ_1 and ϕ_2 contribute to the sheath voltage [46].

In most cases, the excitation rate follows similar patterns as the ionization rate. Therefore, it is possible to compare and validate our simulation data with experimental results obtained by PROES. The results of such measurements, carried out in a discharge operated at $f_1 = 1.937$ MHz and $f_2 = 27.12$ MHz ($f_2/f_1 = 14$) in helium gas with small admixture of O$_2$ and Ne [92] are shown in figure 10(*a*). As explained in section 2.3, Ne is admixed as the tracer gas for PROES. Optical access is provided by a transparent optical block made of quartz, which is implemented into confinement rings used to ensure a symmetric discharge [92]. O$_2$ is admixed (i) to avoid parasitic coatings caused by material sputtered from the electrodes on this optical block that would limit the optical access to the plasma and (ii) to stabilize the discharge. None of these admixtures are expected to affect the electron heating and excitation dynamics qualitatively. The corresponding PIC/MCC simulation results assuming pure He buffer gas and using $\phi_1 = 800$ V and $\phi_2 = 550$ V, $p = 65$ Pa, and $L = 1.2$ cm [52] are shown in figure 10(*b*)—these assume $\gamma = 0.45$, $R = 0.2$, and $T_g = 400$ K. Electron beams, which are launched toward the bulk at phases of sheath expansion,
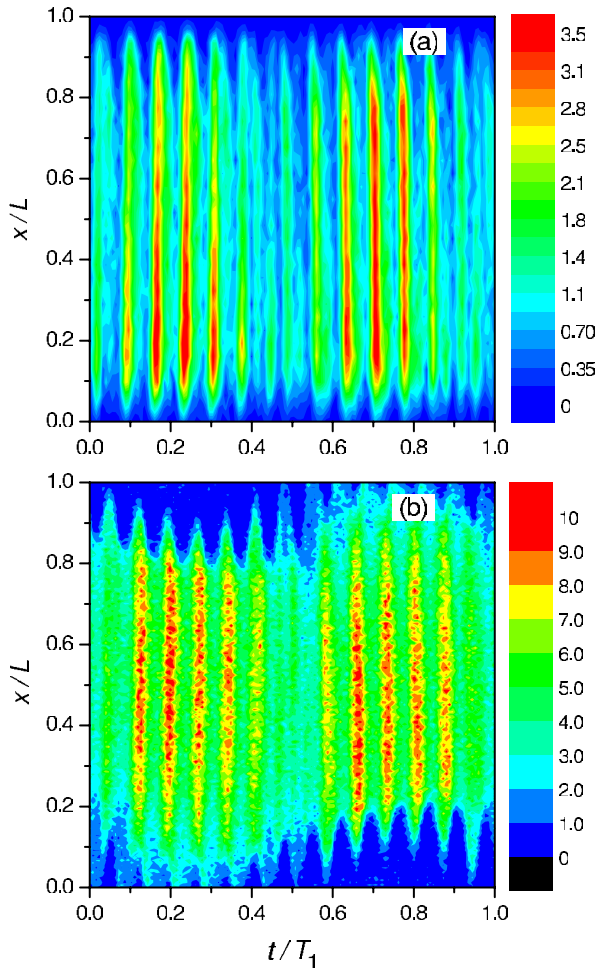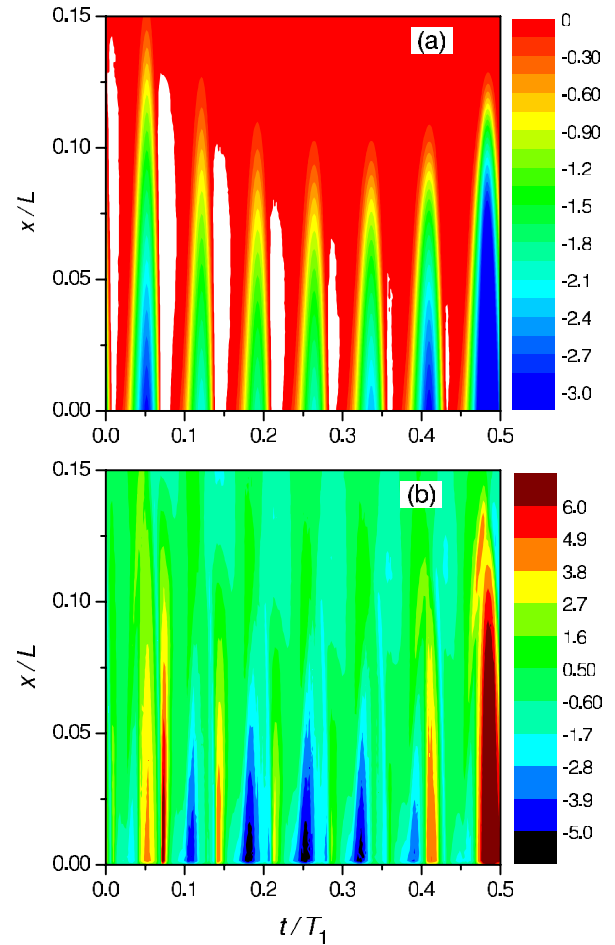
Figure 10. (*a*) Experimentally determined spatio-temporal electron-impact excitation into the Ne 2p1 state at 65 Pa [92]. (*b*) Spatio-temporal excitation rate resulting from the PIC/MCC simulation (He, 65 Pa, $\phi_1 = 800$ V and $\phi_2 = 550$ V, $\gamma = 0.45$, $R = 0.2$ and $T_g = 400$ K). The powered electrode is situated at $x = 0$. Reproduced with permission from [52]. Copyright by IOP Publishing.

Figure 11. Spatio-temporal distribution of the electric field (*a*) and the electron heating rate (*b*) resulting from the PIC/MCC simulation of a He discharge at a pressure of 65 Pa, $\phi_1 = 800$ V and $\phi_2 = 550$ V, $\gamma = 0.45$, $R = 0.2$ and $T_g = 400$ K. In (*a*), white regions indicate the reversal of the electric field. The powered electrode is situated at $x = 0$. (*a*) is reproduced with permission from [52]. Copyright by IOP Publishing.

can clearly be recognized in both panels of figure 10. There is a very good agreement between the experimental and the simulation results.

As mentioned above, electric field reversals can occur during sheath collapse. To illustrate this, the electric field distribution and the electron heating rate in helium for the same conditions as above are depicted in figure 11. These plots show only half of the low-frequency (f_1) cycle and only the spatial region limited to the maximum sheath extension at the powered electrode. Electric field reversals, $E > 0$, indicated with white color in figure 11(*a*), appear whenever the high-frequency sheath is retracted, to accelerate electrons toward the electrode [18].

3.3. Electrically asymmetric multi-frequency discharges

In figure 12 we compare the dependence of the dc self-bias voltage, the mean ion energy, and the ion flux on the phase difference between the driving harmonics, as obtained experimentally (reported in [49]) and from our present
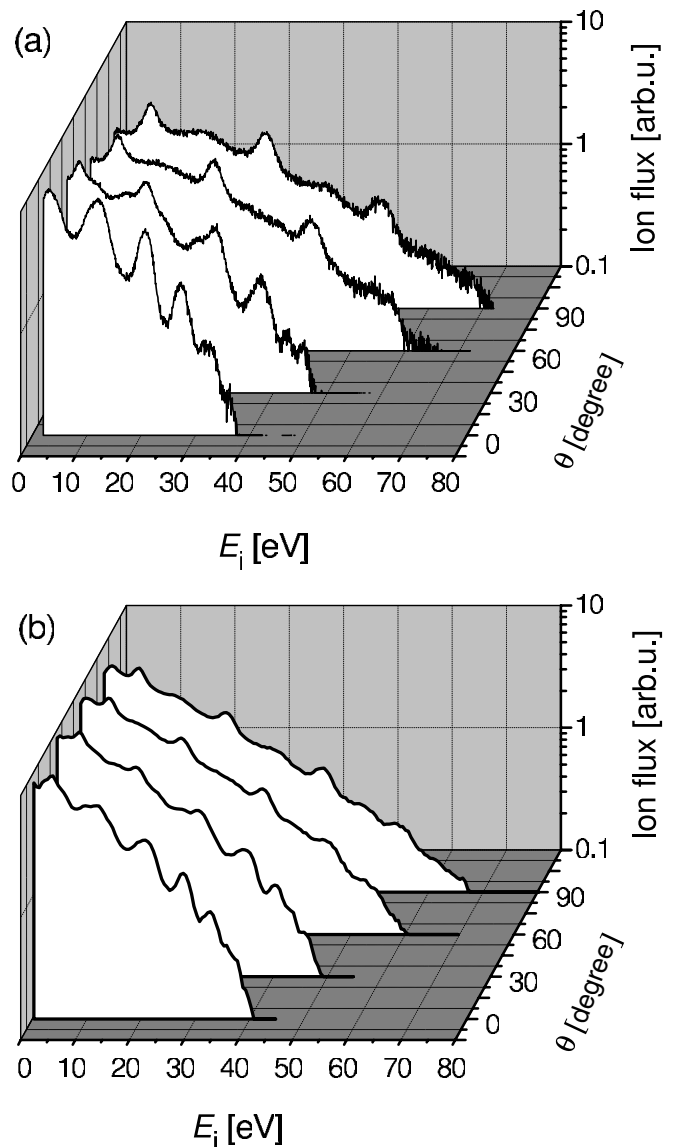
PIC/MCC simulations for a DF EAE discharge operated at $f_1 = 13.56$ MHz and $f_2 = 2f_1$. The discharge conditions are: $p = 20$ Pa (argon), $L = 1$ cm, $\phi_1 = \phi_2 = 76$ V. We note that while the same absolute value of the dc self-bias is obtained in the simulations for the minimum and the maximum, a small shift into the negative direction occurs in the experiment. This is caused by a slight asymmetry of the discharge cell originating from a parasitic capacitive coupling between the glass cylinder confining the plasma and the grounded chamber wall. Nonetheless, there is a very good agreement between the two data sets, with differences amounting less than 10%. A bigger difference is seen in the control range of the mean ion energy. This difference may be attributed to an underestimation of the low energy part of the distribution function in the experiment, e.g., due to defocusing effects or the angle selectivity of the ion energy analyzer (PPM). (In the PIC/MCC simulations the ion energy distribution is calculated regardless of the angular distribution of the ions, while this may play a role in the experiment.) Other reasons might be related to the PIC/MCC simulations, such as the difficulty of obtaining the same plasma density
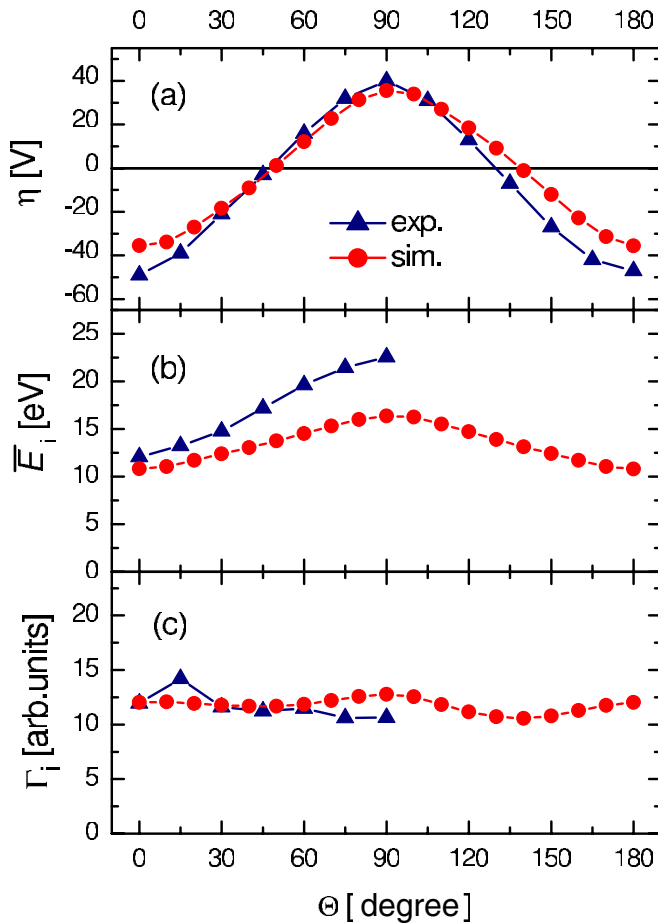
Figure 12. Comparison of experimental and simulation results for dependence of (*a*) the self-bias voltage, (*b*) the mean ion energy and (*c*) the ion flux, on the phase angle Θ at the grounded electrode of an argon discharge at $p = 20$ Pa, $L = 1$ cm, $\phi_1 = \phi_2 = 76$ V. $T_g = 350$ K was used in the simulation. The experimental data are taken from [49].

Figure 13. Comparison of experimental (*a*) and simulation (*b*) results for dependence of the ion flux-energy distribution on the phase angle Θ at the grounded electrode of an argon discharge at $p = 20$ Pa, $L = 1$ cm, $\phi_1 = \phi_2 = 76$ V. The experimental data are taken from [49].

and, accordingly, the same sheaths widths and collisionality as in the experiment and uncertainties in the cross section data sets, which are typically most pronounced in the low energy region. The ion flux again shows very similar behavior as a function of Θ. The absolute ion flux is not known in the experiment. Hence, the experimental data were scaled to match the calculated flux. Figure 12(*c*) confirms that the ion flux is rather insensitive on the phase angle—both in the experiments and in the simulations—allowing independent control of ion properties in DF discharges using the EAE.

The flux-energy distribution of Ar$^+$ ions at selected phase angles and under the same conditions as before are displayed in figure 13. We find a very good overall agreement between the results of experiment and simulation; the shapes of the distributions, the appearance of the peaks and the cutoff energies are quite close. However, in accordance with the discussion of the mean ion energy given above, it can be observed that the low energy part of the distribution function is slightly larger in the simulations compared with the experiment. Furthermore, a closer observation would point out some differences in the exact positions of the peaks, as well as in their relative amplitudes. These may originate again

from the peculiarities of the PPM that are not accounted for in the simulations and from the imperfections of the discharge model that we use. The agreement is however, more than satisfactory.

The self-excitation of PSR oscillations is a fundamental phenomenon of asymmetric CCRF discharges operated at low pressures. The asymmetry may be caused by the geometrical configuration or the application of an asymmetric voltage waveform to the plasma. Therefore, using the EAE the discharge current exhibits resonance oscillations even in geometrically symmetric discharges, if the symmetry parameter ε strongly differs from unity. The PSR and its effect on the electron heating have been investigated in DF cases via simulations [15, 85], experiments [85], as well as theoretical descriptions [16, 54, 85]. It can be expected that the self-excitation of the PSR is even more pronounced
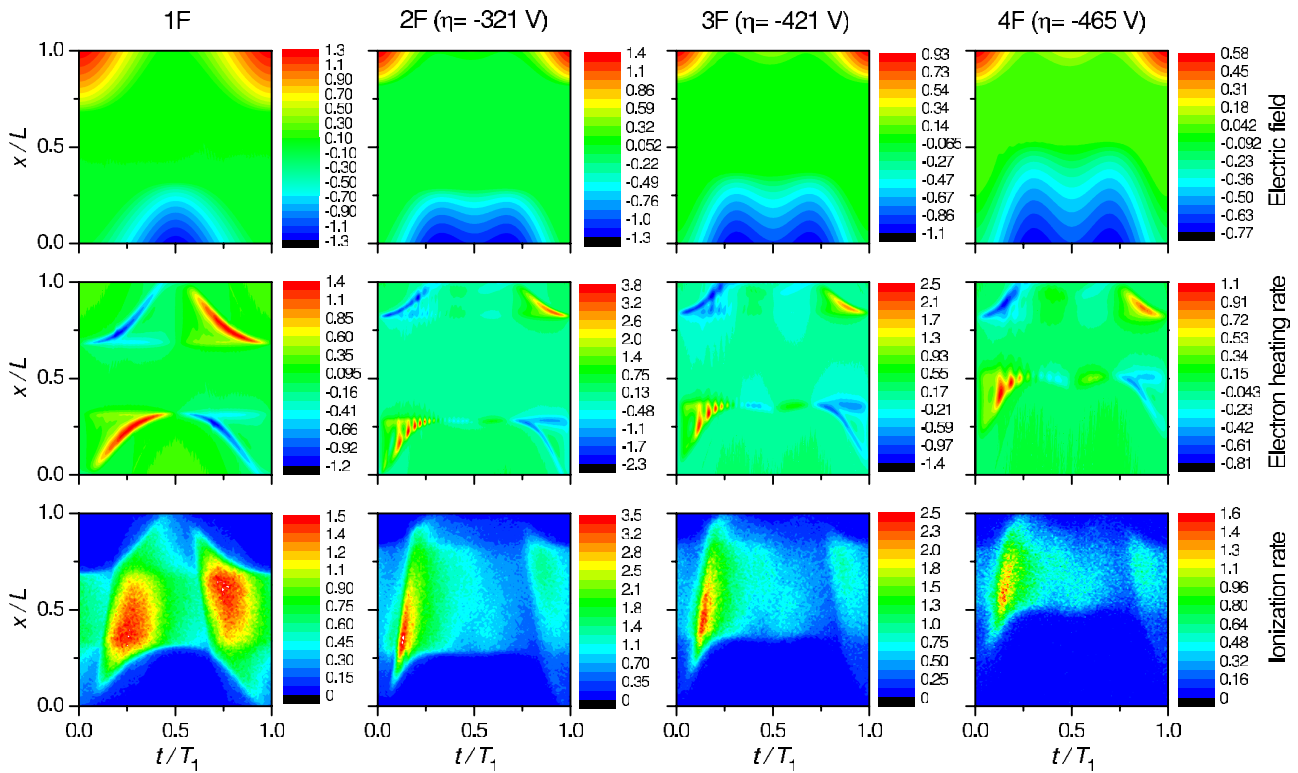
Figure 14. Spatio-temporal distributions of the electric field (upper row), the electron heating rate (middle row), and the ionization rate (bottom row) in argon discharges driven by different number of harmonics indicated above the columns. The units are 10^5 V m^{-1} for the electric field, 10^5 W m^{-3} for the heating rate and 10^{15} cm^{-3}s^{-1} for the ionization rate. $p = 3$ Pa, $L = 3$ cm, $\sum \phi_k = 800$ V.

in electrically asymmetric discharges driven by multiple frequencies, since the induced asymmetry can be significantly enhanced [51].

Figure 14 shows the spatio-temporal distributions of the electric field, the electron heating rate, and the ionization rate in argon discharges driven by different number of harmonics, from $N = 1$ to $N = 4$, at $p = 3$ Pa, $L = 3$ cm, $\gamma = 0.2$, $T_g = 400$ K. Here, the voltage amplitudes are not chosen equally but calculated by the following expression, which was proven to yield the maximum possible self-bias [50]:

$$\phi_k = \phi_{tot} \frac{N - k + 1}{N}. \tag{10}$$

In the case of DF excitation, e.g., this gives $\phi_1 = \frac{2}{3}\phi_{tot}$ and $\phi_2 = \frac{1}{3}\phi_{tot}$. The total voltage amplitude is kept constant at $\phi_{tot} = 800$ V and all phase angles are set to zero, $\Theta_k = 0°$. The number of harmonics, as well as the calculated self-bias voltage is indicated above the columns of figure 14. As expected, the magnitude of η increases with increasing number of the harmonics [51].

At single-frequency operation the well known patterns of the distributions are obtained. At $N > 1$, however, additional features show up in the electron heating rate, which are manifestations of the PSR oscillations appearing due to the electrically induced asymmetry. We also note that the domain of high ionization shrinks, when the number of harmonics is increased and the bulk length decreases due to the increasing length of the sheath at the powered electrode. The frequency of the PSR oscillations decreases and less

maxima can be observed with increasing number of applied harmonics.

4. Summary

In this paper, we have illustrated the basic features of capacitively coupled RF discharges excited by one, two or multiple frequencies. A combination of PIC/MCC simulation results, experimental data and theoretical modeling has been presented.

In the case of single-frequency capacitive discharges, three fundamental mechanisms of electron heating and discharge sustainment were shown and explained: (i) acceleration of electrons during sheath expansion (α-mode), (ii) multiplication of secondary electrons inside the expanded sheath (γ-mode), (iii) electrons interacting with electric fields inside the plasma bulk and around the sheath edges in electronegative plasmas (DA-mode). The dependence of the shape of the ion flux-energy distributions at the electrodes on global parameters, i.e. pressure and frequency, and the limitations of controlling plasma properties in single-frequency discharges have been discussed.

The way how to control the shape of the ion flux-energy distributions in classical dual-frequency discharges has been presented: the transition between a single peaked (pure high-frequency discharge) and a broad distribution for high amplitudes of the low-frequency component, which is slow enough to allow the ions to respond, was examined. It was shown that separate control of the total ion flux and mean ion

energy is possible only within a narrow window of discharge operating conditions. The reasons for the changes in the ion flux as a function of the amplitude of the low-frequency component were found in the simulations and experiments to be the frequency coupling of the sheath motion and the effect of secondary electrons, both affecting the electron heating and ionization. An example of the field reversal was given to illustrate the manifold features of electron dynamics.

The electrical asymmetry effect offers a completely different way to control the mean ion energy independently of the ion flux: two (or more) consecutive harmonics are applied, allowing to control the discharge symmetry and subsequent properties via the phase angle(s) between the frequencies. A comparison of simulation and experimental data summarized previous investigations and demonstrated, how the dc self-bias, that develops due to the electrical asymmetry, and the mean ion energy can be adjusted without changing the total ion flux by more than a few percent. The experimentally obtained ion flux-energy distribution functions agreed quite well with the simulation results. The self-excitation of plasma series resonance oscillations was studied in geometrically symmetric electrically asymmetric multi-frequency discharges operated at low pressures. The occurrence of the PSR in the discharge current can be reproduced and explained by the analytical model, whereas the PIC/MCC simulation gives more insights into the emerging spatio-temporal electron heating structures.

Acknowledgments

References

[1] Makabe T and Petrović Z Lj 2006 *Plasma Electronics: Applications in Microelectronic Device Fabrication* (London: Taylor and Francis)

[2] Lieberman M A and Lichtenberg A J 2005 *Principles of Plasma Discharges and Materials Processing* 2nd edn (New York: Wiley-Interscience)

[3] Park G Y, Park S J, Choi I G, Koo I G, Byun J H, Hong J W, Sim J Y, Collins G J and Lee J K 2012 *Plasma Sources Sci. Technol.* **21** 043001

Benedikt J, Hofmann S, Knake N, Bottner H, Reuter R, von Keudell A and Schulz-von der Gathen V 2010 *Euro. Phys. J.* D **60** 539

Knake N, Reuter S, Niemi K, Schulz-von der Gathen V and Winter J 2008 *J. Phys. D: Appl. Phys.* **41** 194006

Hemke T, Wollny A, Gebhardt M, Brinkmann R P and Mussenbrock T 2011 *J. Phys. D: Appl. Phys.* **44** 285206

[4] Shihab M, Ziegler D, and Brinkmann R P 2012 *J. Phys. D: Appl. Phys.* **45** 185202

[5] Kawamura E, Vahedi V, Lieberman M A and Birdsall C K 1999 *Plasma Sources Sci. Technol.* **8** R45

[6] Jacobs B, Gekelman W, Pribyl P and Barnes M 2011 *Phys. Plasmas* **18** 053503

[7] Belenguer Ph and Boeuf J-P 1990 *Phys. Rev.* A **41** 4447

[8] Lieberman M A and Godyak V A 1998 *IEEE Trans. Plasma Sci.* **26** 955

Godyak V A and Piejak R B 1990 *Phys. Rev. Lett.* **65** 996

Turner M M 2009 *J. Phys. D: Appl. Phys.* **42** 194008

Schulze J, Heil B G, Luggenhölscher D, Brinkmann R P and Czarnetzki U 2008 *J. Phys. D: Appl. Phys.* **41** 195212

Schulze J, Heil B G, Luggenhölscher D, Mussenbrock T, Brinkmann R P and Czarnetzki U 2008 *J. Phys. D: Appl. Phys.* **41** 042003

[9] Vender D and Boswell R W 1992 *J. Vac. Sci. Technol.* A **10** 1331

[10] Annaratone B M, Ku V P T, Allen J E 1995 *J. Appl. Phys.* **77** 5455

Klick M 1996 *J. Appl. Phys.* **79** 3445

Schulze J, Kampschulte T, Luggenhölscher D and Czarnetzki U 2007 *J. Phys. Conf. Ser.* **86** 012010

[11] Czarnetzki U, Mussenbrock T and Brinkmann R P 2006 *Phys. Plasmas* **13** 123503

[12] Mussenbrock T and Brinkmann R P 2006 *Appl. Phys. Lett.* **88** 151503

[13] Lieberman M A, Lichtenberg A J, Kawamura E, Mussenbrock T and Brinkmann R P 2008 *Phys. Plasmas* **15** 063505

Mussenbrock T, Brinkmann R P, Lieberman M A, Lichtenberg A J and Kawamura E 2008 *Phys. Rev. Lett.* **101** 085004

[14] Ziegler D, Mussenbrock T and Brinkmann R P 2009 *Phys. Plasmas* **16** 023503

[15] Donkó Z, Schulze J, Czarnetzki U and Luggenhölscher 2009 *Appl. Phys. Lett.* **94** 131501

[16] Bora B, Bhuyan H, Favre M, Wyndham E, and Chuaqui H 2012 *Appl. Phys. Lett* **100** 094103

[17] Gans T, Lin Chun C, Schulz-von der Gathen V, Döbele F 2003 *Phys. Rev.* A **67** 012707

[18] Sato A H and Lieberman M A 1990 *J. Appl. Phys.* **68** 6117

Czarnetzki U, Luggenhölscher D and Döbele H F 1999 *Plasma Sources Sci. Technol.* **8** 230

Schulze J, Donkó Z, Heil B G, Luggenhölscher D, Mussenbrock T, Brinkmann R P and Czarnetzki U 2008 *J. Phys. D: Appl. Phys.* **41** 105213

[19] Phelps A V, Petrović Z Lj 1999 *Plasma Sources Sci. Technol.* **8** R21

[20] Böhm C and Perrin J 1993 *Rev. Sci. Instrum.* **64** 31

[21] Schulze J, Derzsi A, Dittmann K, Hemke T, Meichsner J, Donkó Z 2011 *Phys. Rev. Lett.* **107** 275001

[22] Boeuf J P 1992 *Phys. Rev.* A **46** 7910

Belenguer Ph, Blondeau J Ph, Boufendi L, Toogood M, Plain A, Bouchoule A, Laure C and Boeuf J P 1992 *Phys. Rev.* A **46** 7923

[23] Lieberman M A, Booth J P, Chabert P, Rax JM and Turner M M 2002 *Plasma Sources Sci. Technol.* **11** 283

Chabert P 2007 *J. Phys. D: Appl. Phys.* **40** R63

[24] Coburn J W and Kay E 1972 *J. Appl. Phys.* **43** 4965

Lieberman M A and Savas S E 1990 *J. Vac. Sci. Technol.* A **8** 1632

[25] Kitajima T, Takeo Y, Petrović Z Lj and Makabe T 2000 *Appl. Phys. Lett.* **77** 489

[26] Denda T, Miyoshi Y, Komukai Y, Goto T, Petrovic Z L and Makabe T 2004 *J. Appl. Phys.* **95** 870

[27] Georgieva V and Bogaerts A 2006 *Plasma Sources Sci. Technol.* **15** 368

[28] Lee S H, Tiwari P K and Lee J K 2009 *Plasma Sources Sci. Technol.* **18** 025024

[29] Mussenbrock T, Ziegler D and Brinkmann R P 2006 *Phys. Plasmas* **13** 083501

[30] Kawamura E, Lieberman M A and Lichtenberg A J 2006 *Phys. Plasmas* **13** 053506

[31] Boyle P C, Ellingboe A R and Turner M M 2004 *Plasma Sources Sci. Technol.* **13** 493

[32] Wang S-B and Wendt A E 2000 *J. Appl. Phys.* **88** 643

Patterson M M, Chu H-Y and Wendt A E 2007 *Plasma Sources Sci. Technol.* **16** 257

[33] Johnson E V, Verbeke T, Vanel J C and Booth J P 2010 *J. Phys. D: Appl. Phys.* **43** 412001

[34] Rauf S and Kushner M J 1999 *IEEE Trans. Plasma Sci.*
27 1329
Dudin S V, Zykov A V, Polozhii K I and Farenik V I 1998
Tech. Phys. Lett. **24** 881
[35] Kawamura E, Lieberman M A, Lichtenberg A J and
Hudson E A 2007 *J. Vac. Sci. Technol.* A **25** 1456
Kawamura E, Lichtenberg A J and Lieberman M A 2008
Plasma Sources Sci. Technol. **17** 045002
[36] Jiang W, Xu X, Dai Z L and Wang Y N 2008 *Phys. Plasmas*
15 033502
[37] Guan Z-Q, Dai Z-L and Wang Y-N 2005 *Phys. Plasmas*
12 123502
[38] O'Connell D, Gans T, Semmler E and Awakowicz P 2008
Appl. Phys. Lett. **93** 081502
[39] Ziegler D, Trieschmann J, Mussenbrock T, Brinkmann R P,
Schulze J, Czarnetzki U, Semmler E, Awakowicz P,
O'Connell D and Gans T 2010 *Plasma Sources Sci.
Technol.* **19** 045001
[40] Schulze J, Gans T, O'Connell D, Czarnetzki U, Ellingboe A R
and Turner M M 2007 *J. Phys. D: Appl. Phys.* **40** 7008
[41] Gans T, Schulze J, O'Connell D, Czarnetzki U, Faulkner R,
Ellingboe A R and Turner M M 2006 *Appl. Phys. Lett.*
89 261502
[42] Turner M M and Chabert P 2006 *Phys. Rev. Lett.*
96 261502
[43] Waskoenig J and Gans T 2010 *Appl. Phys. Lett.* **96** 181501
[44] Donkó Z 2007 *Proc. Symp. of Application of Plasma
Processes (Podbanske, Slovakia, 20–25 January, 2007)*
eds J Matuska *et al* IL02, p 21
[45] Booth J P, Curley G, Marić D and Chabert P 2010 *Plasma
Sources Sci. Technol.* **19** 015005
[46] Donkó Z, Schulze J, Hartmann P, Korolov I, Czarnetzki U and
Schüngel E 2010 *Appl. Phys. Lett.* **97** 081501
[47] Heil B G, Schulze J, Mussenbrock T, Brinkmann R P
and Czarnetzki U 2008 *IEEE Trans. Plasma Sci.*
36 1404
Heil B G, Czarnetzki U, Brinkmann R P and Mussenbrock T
2008 *J. Phys. D: Appl. Phys.* **41** 165202
[48] Donkó Z, Schulze J, Heil B G and Czarnetzki U 2009 *J. Phys.
D: Appl. Phys.* **42** 025205
[49] Schulze J, Schüngel E and Czarnetzki U 2009 *J. Phys. D:
Appl. Phys.* **42** 092005
[50] Schulze J, Schüngel E, Czarnetzki U and Donkó Z 2009
J. Appl. Phys. **106** 063307
[51] Schulze J, Schüngel E, Donkó Z and Czarnetzki U 2011
Plasma Sources Sci. Technol. **20** 015017
[52] Schulze J, Donkó Z, Luggenhölscher D and Czarnetzki U
2009 *Plasma Sources Sci. Technol.* **18** 034011
[53] Longo S and Diomede P 2009 *Plasma Process. Polym.*
6 370
[54] Schüngel E, Zhang Q-Z, Iwashita S, Schulze J, Hou L-J,
Wang Y-N and Czarnetzki U 2011 *J. Phys. D: Appl. Phys.*
44 285205
[55] Schulze J, Derzsi A and Donkó Z 2011 *Plasma Sources Sci.
Technol.* **20** 024001
[56] Schulze J, Donkó Z, Schüngel E and Czarnetzki U 2011
Plasma Sources Sci. Technol. **20** 045007
[57] Johnson E V, Delattre P A and Booth J P 2012 *Appl. Phys. Lett*
100 133504
[58] Lafleur T, Boswell R W and Booth J P 2012 *Appl. Phys. Lett.*
100 194101
[59] Iwashita S, Uchida G, Schulze J, Schüngel E, Hartmann P,
Shiratani M, Donkó Z and Czarnetzki U 2012 *Plasma
Sources Sci. Technol.* **21** 032001
[60] Birdsall C K and Langdon A B 1985 *Plasma Physics via
Computer Simulation* (New York: McGraw-Hill)
[61] Hockney R W and Eastwood J W 1981 *Computer Simulation
Using Particles* (New York: McGraw-Hill)
[62] Birdsall C K 1991 *IEEE Trans. Plasma Science* **19** 65
[63] Phelps A V 1994 *J. Appl. Phys.* **76** 747
[64] Longo S, Gorse C and Capitelli M 1991 *IEEE Trans. Plasma
Sci.* **19** 379
Longo S and Capitelli M 1994 *Plasma Chem. Plasma Process.*
14 1–13
[65] Kurihara M, Petrović Z Lj and Makabe T 2000 *J. Phys. D:
Appl. Phys.* **33** 2146
[66] Donkó Z and Petrović Z Lj 2007 *J. Phys.: Conf. Ser.*
86 012011
[67] Verboncoeur J P 2005 *Plasma Phys. Control. Fusion* **47** A231
[68] Matyash K, Schneider R, Taccogna F, Hatayama A, Longo S,
Capitelli M, Tskhakaya D and Bronold F X 2007 *Contrib.
Plasma Phys.* **47** 595
[69] Tskhakaya D, Matyash K, Schneider R and Taccogna F 2007
Contrib. Plasma Phys. **47** 563
[70] Turner M M 2006 *Phys. Plasmas* **13** 033506
[71] Vahedi V, DiPeso G, Birdsall C K, Lieberman M A and
Rognlien T D 1993 *Plasma Sources Sci. Technol.* **2** 261
[72] Donkó Z 2011 *Plasma Sources Sci. Technol.* **20** 024001
[73] Lister G G 1992 *J. Phys. D: Appl. Phys.* **25** 1649
[74] Koenig H R and Maissel L I 1970 *IBM J. Res. Dev.* **14** 168
[75] Godyak V A and Sternberg N 1990 *Phys. Rev.* A **42** 2299
[76] Misium G R, Lichtenberg A J and Lieberman M A 1989
J. Vac. Sci. Technol. A **7** 1007
[77] Metze A, Ernie D W and Oskam H J 1986 *J. Appl. Phys.*
60 3081
[78] Song Y P, Field D and Klemperer D F 1990 *J. Phys. D: Appl.
Phys.* **23** 673
[79] Franklin R N and Snell J 1999 *J. Phys. D: Appl. Phys.* **32** 2190
[80] Dewan M N A, McNally P J and Herbert P A F 2002 *J. Appl.
Phys.* **91** 5604
[81] Boyle P C, Robiche J and Turner M M 2004 *J. Phys. D: Appl.
Phys.* **37** 1451
[82] Pointu A M 1986 *J. Appl. Phys.* **60** 4113
[83] Raizer Yu P and Shneider M N 1992 *Plasma Sources Sci.
Technol.* **1** 102
[84] Sobolewski M A 1997 *Phys. Rev.* E **56** 1001
[85] Czarnetzki U, Schulze J, Schüngel E, Donkó Z 2011 *Plasma
Sources Sci. Technol.* **20** 024010
[86] Schulze J, Schüngel E, Donkó Z, Luggenhölscher D and
Czarnetzki U 2010 *J. Phys. D: Appl. Phys.* **43** 124016
Dittmann K, Drozdov D, Krames B and Meichsner J 2007
J. Phys. D: Appl. Phys. **40** 6593
[87] Denpoh K and Nanbu K 2000 *Japan. J. Appl. Phys.* **39** 2804
[88] Voloshin D, Proshina O and Rakhimova T 2010 *J. Phys. Conf.
Series* **207** 012026
[89] Wild C and Koidl P 1991 *J. Appl. Phys.* **69** 2909
[90] Georgieva V and Bogaerts A 2005 *J. Appl. Phys.* **98** 023308
[91] Boyle P C, Ellingboe A R and Turner M M 2004 *J. Phys. D:
Appl. Phys.* **37** 697
[92] Schulze J, Gans T, O'Connell D, Czarnetzki U,
Ellingboe A R and Turner M M 2007 *J. Phys. D: Appl.
Phys.* **40** 7008